

1     **Granulometric characterization of paleosols in loess series by automated static image**  
2   **analysis**

3  
4     György Varga<sup>1,\*</sup>, János Kovács<sup>2,3</sup>, Zoltán Szalai<sup>1,4</sup>, Csaba Cserhádi<sup>5</sup>, Gábor Újvári<sup>6</sup>

5  
6     <sup>1</sup>Geographical Institute, Research Centre for Astronomy and Earth Sciences, Hungarian  
7     Academy of Sciences, Budaörsi út 45, H-1112 Budapest, Hungary

8     <sup>2</sup>Department of Geology & Meteorology, University of Pécs, Ifjúság u. 6, H-7624 Pécs,  
9     Hungary

10    <sup>3</sup>Environmental Analytical & Geoanalytical Research Group, Szentágothai Research  
11    Centre, University of Pécs, Ifjúság u. 20, H-7624 Pécs, Hungary

12    <sup>4</sup>Department of Environmental and Landscape Geography (Institute of Geography and Earth  
13    Sciences, Faculty of Science), Eötvös University, Pázmány Péter sétány 1/c, H-1117 Budapest,  
14    Hungary

15    <sup>5</sup>Department of Solid State Physics, University of Debrecen, Bem tér 18/b, H-4026 Debrecen,  
16    Hungary

17    <sup>6</sup>Institute for Geological and Geochemical Research, Research Centre for Astronomy and Earth  
18    Sciences, Hungarian Academy of Sciences, H-1112 Budapest, Budaörsi u. 45., Hungary

19

20    \*corresponding author; e-mail: [varga.gyorgy@csfk.mta.hu](mailto:varga.gyorgy@csfk.mta.hu)

21

22

23

24    **Abstract**

25

26 An automated image analysis method is proposed here to study the size and shape of siliciclastic  
27 sedimentary particles of paleosols of Central European loess sequences. Several direct and  
28 indirect measurement techniques are available for grain size measurements of sedimentary  
29 mineral particles. Indirect techniques involve the use of some kind of physical laws, however,  
30 all requirements for calculations are in many cases not known. Even so, the direct manual  
31 microscopic observation and measurement of large, representative number of grains is time-  
32 consuming and sometimes rather subjective. Therefore, automated image analyses techniques  
33 provide a new and perspective way to analyse grain size and shape sedimentary particles.

34 Here we test these indirect and direct techniques and provide new granulometric data of  
35 paleosols. Our results demonstrate that grain size data of the mineral dust samples are strongly  
36 dependent on shape parameters of particles, and shape heterogeneity was different of the  
37 different size classes. Due to the irregular grain shape parameters, uncertainties have arisen also  
38 for the sizes.

39 In this paper we present a possible correction procedure to reduce the differences among the  
40 results of the laser diffraction and image analysis methods. By applying new correction factors,  
41 results of the two approaches could be get closer but the most definite factor, the unknown  
42 thickness of particles remained a problem to solve. The other presented method to assess the  
43 uncertain 3<sup>rd</sup> dimension of particles by their intensity-size relationships makes us able to reduce  
44 further the deviations of the two sizing methods.

45

46 **Keywords:** image analyses, particle shape, grain size, paleosols

47

48 **Introduction**

49

50 Determination of granulometric parameters has been a major focus of sedimentary studies and  
51 is of growing interest in the Earth sciences (Vandenberghe et al., 2013, 2018; Újvári et al.,  
52 2016). There is a variety of instrumental techniques for the measurement of particle size. These  
53 include sieve and pipette methods through laser scattering to image analysis of pictures taken  
54 by optical or scanning electron microscopes. These various analytical methods are based on  
55 different approaches to measuring particle size. In sieving, the second largest dimension is  
56 measured as particles orientate themselves to optimally pass through the mesh, and grain size  
57 distributions are calculated from the mass of particles within different size classes (Ludwick  
58 and Henderson, 1968). Techniques based on the settling velocity of suspended particles assume  
59 that larger/heavier particles settle more rapidly from suspension than smaller/lighter ones.  
60 Particle size information of sedimentary deposits is usually determined by laser diffraction  
61 devices. This is a robust method yielding much more accurate and reliable information on grain  
62 size of windblown sediments than sieving or the gravimetric methods (Konert and  
63 Vandenberghe, 1997; Di Stefano et al., 2010; Fisher et al., 2017; Makó et al., 2017). However,  
64 grain size data obtained with these measurements simply result from indirect estimations of  
65 sphere equivalent diameters, as calculated from the acquired laser light scattering data using  
66 mathematical transformations of different optical models (Fraunhofer and Mie theories).  
67 Grain size characterization of irregular shaped three-dimensional sedimentary particles is a  
68 complex problem. The size of such particles is approximated by using equivalent diameters, so  
69 that the real irregular particle is replaced with an imaginary sphere or circle having similar  
70 volume, surface or area (Fisher et al., 2017) . This means that sphere equivalent (SE) or circle  
71 equivalent (CE) diameters are used instead of other size parameters. However, size description  
72 of a non-spherical particle using simple indices (SE or CE diameter) consequently leads to  
73 oversimplifications.

74 Not only size, but shape parameters of particles hold vital information on sedimentary transport  
75 and deposition mechanisms and post-depositional, environment-related alterations (Mazzullo  
76 et al., 1992; Pye, 1994). As the terms particle morphology, form and shape have been used in a  
77 variety of ways in published papers (Benn and Ballantyne, 1993), here, particle shape includes  
78 relative dimensions of particles, overall smoothness of particle outline and roughness.  
79 Traditional image analysis techniques have been applied widely, however previously published  
80 studies have been carried out on populations with much smaller number of particles compared  
81 to automated analyses (e.g. Dellino and La Volpe, 1996; Bagheri et al., 2015; Liu, et al., 2015).  
82 Measurement of particle shape is time-consuming (Tafesse et al., 2013). Automated static  
83 image analysis is still uncommon and underexploited for particle size and shape distribution  
84 analysis of sediments. The use of automated digital image analysis solves the issues generated  
85 by low number of measured particles as it is more precise, less time-consuming and easier to  
86 use compared with traditional methods (Baptista et al., 2012; Rodríguez et al., 2013; Campaña  
87 et al., 2016). The average particle number of automated imaging amounts to ca.  $10^4$ - $10^6$   
88 particles, which allows us to gain statistically robust and objective insights into the  
89 morphological characteristics of particles. Various size and shape parameters, as well as optical  
90 intensity values of each particle, are routinely measured and number-size distributions can  
91 easily be converted to volumetric distributions, thus the direct comparison with results obtained  
92 by laser diffraction can be done. To date, only a few studies have been published on automated  
93 image analyses of particle size and particle shape parameters of sedimentary deposits (Rubin,  
94 2004; Graham et al., 2005; Warrick et al., 2009; Buscombe et al., 2010), and therefore much  
95 uncertainty exists about the relationship between the different methods. Shang et al. (in press)  
96 presented grain size and shape results obtained by dynamic image analysis of Chinese loess and  
97 red clay samples.

98 In this study paleosols embedded in Central European loess sequences were investigated in  
99 detail as they are the product of a complex depositional environment: granulometric  
100 characteristics of paleosols are dependent on (1) the grain size properties of the underlying  
101 windblown loess material from which the soil was formed; (2) post-depositional alteration  
102 governed by the weathering intensity characteristic for the given interstadial/interglacial period;  
103 and (3) possible syn-sedimentary dust material additions (and/or removal). However, it must be  
104 emphasized that this study is not aimed at obtaining genetically meaningful sedimentary  
105 interpretations of the samples, but instead (1) compares the grain size results obtained by widely  
106 used laser diffraction technique and by a new, high-precision granulometric characterization  
107 approach, namely automated static image analysis; (2) discusses the major differences and  
108 underlying causes; and (3) identifies problematic issues of grain size and shape determinations  
109 of the automated static image analysis technique.

110 Details of physicochemical environment of entrainments, transport, accumulation and post-  
111 depositional alterations of sedimentary particles can partly be reconstructed using proxies of  
112 grain size and various grain shape parameters (e.g. particle circularity, convexity, relative  
113 lengths of orthogonal axes) of sediments (Weltje and Prins, 2007; Bokhorst, et al., 2011; van  
114 Hatteren et al., in press; Schulte et al., in press; Schulte and Lehmkuhl, in press; Varga et al., in  
115 press). This is especially true for well sorted aeolian dust deposits with a fairly narrow grain  
116 size range in the silt fraction as a consequence of the selective nature of sediment transport by  
117 wind (Pye, 1987). As terrestrial wind-blown deposits are among the most important archives of  
118 past environmental changes, appropriate explanation and interpretation of proxy data is another  
119 key issue (Varga et al., in press). Various aspects of aeolian sedimentation (wind strength,  
120 source distance and transport modes, etc.) can be estimated from accurate grain size data. Huge  
121 amounts of laser diffraction grain size data have accumulated over the past decades, to make

122 the comparison of new and more detailed image analysis-based granulometric information with  
123 previous researches a comprehensive discussion of methodological differences is needed.

124

## 125 **Materials and Methods**

126

### 127 Geological setting and samples

128

129 Loess deposits cover more than half of the area of the Carpathian Basin in Central Europe  
130 (Oches and McCoy, 1995; Marković et al., 2011, 2015; Újvári et al., 2014). Previous studies  
131 revealed the complex paleoenvironmental development and depositional history of the last ca.  
132 1 million years based on multi-proxy analyses of these excellent archives (Horváth and Bradák,  
133 2014; Újvári et al., 2014; Marković et al., 2015). Changing climatic conditions of Pleistocene  
134 glacial-interglacial periods were imprinted in windblown dust deposition and post-sedimentary  
135 alterations of accumulated sequences. Increased dust flux of dry and cold glacials provided  
136 material for the formation of typical loess deposits. The loess formation periods were  
137 interrupted by soil development during moist and mild interglacials. While the geochemical  
138 composition of loess deposits are fairly homogeneous, climatic and environmental conditions,  
139 duration and intensity of soil forming intervals were more diverse than during glacials, leading  
140 to a geochemically and sedimentary mixed pedostratigraphy of the region (Varga, 2015).  
141 Pedogenesis during interglacials were even more complex, as we have to consider syngenetic  
142 fine-grained dust addition from external source regions (e.g., from the Sahara) to the local  
143 material during accretionary soil formation (Varga et al., 2016).

144 The persistent decreases in weathering intensity during interglacial intervals from the Early  
145 Pleistocene to Holocene were preserved and manifested in different types of paleosols. The

146 Late and younger Middle Pleistocene loess deposits are intercalated by steppe, forest-steppe  
147 and brown forest soils, while the older paleosols are reddish brown, rubified soils.  
148 A generalized loess-paleosol sequence was set-up primarily based on the Paks loess section on  
149 the right bank of River Danube in Hungary (N46° 38' 25" E18° 52' 36"), however, paleosol  
150 units of MIS-5 were missing in this well-studied site (Újvári et al., 2014), reference samples for  
151 the last interglacial period were collected from the Tamási section (Southwest Hungary,  
152 Transdanubian Hills; N46° 37' 6" E18° 16' 32"). Nine representative samples were chosen for  
153 detailed analyses from the sampled key pedostratigraphic units representing MIS-21 up to MIS-  
154 5 interglacial periods (Fig 1). The MIS-13 and MIS-15 soils were excluded from sampling and  
155 subsequent analyses because of their controversial stratigraphic position and truncated  
156 appearance (Oches and McCoy, 1995; Horváth and Bradák, 2014; Újvári et al., 2014; Varga,  
157 2015).

158

#### 159 Samples pre-treatment and grain size measurements

160

161 All samples were chemically pre-treated before granulometric measurements by adapting the  
162 widely used procedure described by Konert and Vandenberghe (1997). Three grams of  
163 sediment were treated with 10 ml H<sub>2</sub>O<sub>2</sub> (30%) and 10 ml HCl (10%) to oxidize organic matter  
164 and dissolve carbonates before laser diffraction measurements. Subsequently, 10 ml of 3.6%  
165 Na<sub>4</sub>P<sub>2</sub>O<sub>7</sub>·10H<sub>2</sub>O was also added to the samples, which were ultrasonicated during the analyses  
166 in order to ensure particle disaggregation. There are two main reasons for carbonate removal:  
167 (1) in loess sediments secondary calcite formation creates coatings among the particles  
168 inhibiting the dispersion of individual grains; (2) separation of detrital and authigenic, post-  
169 depositional carbonates is impossible.

170

171 *Automated static image analysis procedure*

172

173 Granulometric data and Raman spectra were obtained from automatic static image analysis of  
174 Malvern Morphologi G3-ID (Malvern Instruments Ltd., UK), which is an advanced particle  
175 characterization apparatus. This device allows thousands of particle shapes to be quantified in  
176 a few hours and it has recently been used for quality control in the pharmaceutical and mining  
177 industry (Kwan et al., 1999; Ulusoy and Kursun, 2011; Schneider and Marcini, 2013; Gamble  
178 et al., 2014). Nevertheless, only a few studies have exploited image-based methods in  
179 sedimentology so far, apart from preliminary studies designed to demonstrate its potential  
180 (Altuhafi et al., 2012; Polakowski et al., 2014; Duval et al., 2015; Sochan et al., 2015; Campaña  
181 et al., 2016; Nielsen et al., 2016; Polo-Díaz et al., 2016; Becker et al., in press).

182 In this study,  $\sim 7 \text{ mm}^3$  of sedimentary particles were dispersed onto a flat glass slide with an  
183 instantaneous (10 ms) pulse of 4 bar compressed air and 60 s settling time. Particle imaging  
184 was conducted using the  $20\times$  magnification lens ( $960\times$  magnification, 40 pixel per  $\mu\text{m}^2$   
185 resolution) of the Morphologi G3-ID device and z-stacking was enabled (two layers above and  
186 below the focal plane, equivalent to  $27.5 \mu\text{m}$  in total).

187 Size and shape parameters of  $\sim 250,000$  individual particles were automatically recorded by the  
188 software of the Malvern Morphologi G3-ID device for each sample from the captured high-  
189 resolution grayscale images. The most important granulometric parameter of the image analysis  
190 based grain size measurements is the circle-equivalent (CE) diameter of the non-spherical,  
191 irregular-shaped particles. This parameter is calculated as the diameter of a circle with the same  
192 area as the projected two-dimensional particle image. The number-based grain size distribution  
193 is calculated in MATLAB (version R2016a) by classification of every particle into  
194 logarithmically-spaced size classes. Default size-bin allocation of Malvern Mastersizer was  
195 chosen to these calculations to make the comparison of image analyses and laser diffraction



196 results more accurate and representative; particle size data are classified into 101  
197 logarithmically spaced size-bins in the range between 0.01 and 3000  $\mu\text{m}$  (the central value of  
198 the  $i$ th size-bin =  $0.0081^{e^{0.128i}}$ , where  $i=1:101$ ). For transforming number-based distributions  
199 into volume-based distributions CE diameter is used for the calculation of particles volume  
200 (sphere-equivalent [SE] volume) as a weighting factor. The volume of a given size bin is  
201 specified by weighting with the total SE volume of particles classed into this size range.

202 Length and width are estimated from major and minor axes of the particles (Malvern  
203 Instruments Ltd., 2015). The major axis is calculated as a line through the centre of mass of the  
204 two-dimensional projected image at an orientation corresponding to the minimum rotational  
205 energy of the shape. The major axis parameter is the angle of the major axis from a horizontal  
206 line, while the minor axis passes through at a right angle to the major axis. All perimeter points  
207 of the object are projected onto the major axis (minor axis), and the longest distance between  
208 the points is the length (width) of the particle as shown in Fig 2. Other simple grain size  
209 parameters as particle area or perimeter can easily be determined using the acquired images.

210 Grain shape parameters provide additionally information apart from size. Aspect ratio is the  
211 ratio of width and length, while elongation is 1-aspect ratio. The circularity parameter of a  
212 particle describes the proportional relationship between the circumference of a circle equal to  
213 the object's projected area and perimeter. Convexity and solidity are determined using the  
214 convex hull (theoretical rubber band wrapped around the particle – indicated as gray area on  
215 Fig 2) of the two-dimensional images. Convexity is the ratio of perimeter of the convex hull to  
216 the particle perimeter, while solidity is the ratio of the particle and convex hull areas; these are  
217 parameters of the particle edge roughness.

218 Simultaneously, the mean grayscale intensity and standard deviation of particles were also  
219 measured as the bottom light (diascopic) illumination transmits through the particles. White  
220 light intensity of each pixel of particles is recorded on an 8-bit ( $2^8$ ) scale from 0 to 255, where

221 intensity value of zero is white, 255 is black. The automatically recorded dimensionless values  
222 serve as a proxy of optical properties. Mean intensity values are dependent on chemical  
223 composition, mineralogy and particle thickness, while standard deviations of intensities are  
224 controlled by the heterogeneity of particle constitution and surface morphology.

225 Chemical analysis was performed using the built-in Raman spectrometer of the Malvern  
226 Morphologi G3-ID. Spectra were acquired from several hundreds of targeted individual  
227 particles. These were compared with library spectra (BioRad-KnowItAll Informatics System  
228 2017, Raman ID Expert) and correlation calculations were performed to determine the  
229 mineralogy of the targeted sedimentary grains.

230 Image analysis-based measurements were organized into a number-based database. All of the  
231 particles have their own identity number (ID) being the primary key in the data matrix. Each  
232 row represents one particle and columns of the table are size and shape parameters. Large  
233 numbers of measured particles ensure a statistically robust and objective insight into the  
234 granulometric characteristics of the investigated samples.

235

### 236 *Filtering out stacked particles and aggregates*

237

238 Sometimes it can be noticed that particles are not individual grains (see Fig 2d), but are clumps  
239 of particles by natural aggregation of single grains or by artificial stacking of particles during  
240 dispersion onto the glass slide. Using the appropriate shape parameters, these compound objects  
241 can be filtered out. Irregularly aggregated particles often cannot be excluded using only one  
242 parameter. This is why previous studies also applied combinations of intensity and convexity  
243 (Gamble et al., 2011); circularity and convexity (Leibbrandt and Le Pennec, 2015), solidity and  
244 convexity (Liu et al., 2015) to distinguish aggregated particles. As these previous papers were  
245 dealing with microcrystalline cellulose and volcanic ash, morphologically significantly

246 different material than granular particles of paleosols of aeolian dust-derived loess series, in  
247 this study, we applied a new combination of parameters to filter out stacked particles using  
248 elongation (or its complementary, the aspect ratio) and circularity thresholds together. Captured  
249 two-dimensional images of aggregated particles revealed that the perimeters of these rougher  
250 objects are larger than that of individual grains with similar CE-diameter. This observation  
251 formed the basis of application of convexity values in previous studies (Gamble et al., 2011;  
252 Leibbrandt and Le Pennec, 2015; Liu et al., 2015). However, perimeters of two-dimensional  
253 projections of elongated particles can also be significantly higher than those of solid ones due  
254 to circumferential pixels, so particles with low [ $<0.4$ ] elongation (high [ $>0.4$ ] aspect ratio) and  
255 low circularity [ $<0.45$ ] form a class representing stacked or aggregated grains.

256

#### 257 *Sufficient number of measured particles*

258

259 Experiences with automated static image analysis by Malvern Morphologi G3-ID indicate that  
260 scanning of  $\sim 7 \text{ mm}^3$  of sedimentary samples on circular, 60 mm diameter areas of glass slides  
261 provide shape and size parameter information on  $\sim 1$ -1.5 million particles. Since measurements  
262 are time-consuming (average 6-hour measurement time per sample), the generated data-file  
263 sizes are large and impractical, and for cost- and energy-efficiency reasons it seems important  
264 to determine the particle number sufficient for a statistically representative granulometric  
265 characterization. The large number of acquired grain images and obtained parameter data  
266 allowed us to perform a subsampling experiment. Clusters with different numbers of randomly  
267 selected particles were sub-sampled from a total of 1 million measured grains. Every sub-  
268 sample clusters include the results of 100-step iterations of random particle selections.

269

#### 270 *Underestimation of the finest fractions by image analysis: a theoretical approach*

271

272 The measured CE diameter in image analysis is calculated from the two-dimensional images of  
273 particles. It is generally assumed that the instantaneous pulse of compressed air disperses the  
274 sedimentary particles onto the glass slide with a consistent orientation with their largest area  
275 facing to camera. However, this is only one outcome out of infinite possible projections of a  
276 three-dimensional object. During measurements made by dynamic image analysis techniques  
277 these kinds of particle orientation problems do not distort the results since freely falling particles  
278 can rotate freely in all directions (Shang et al., in press).

279 To demonstrate and quantify this distortion, we modelled the deformation of two-dimensional  
280 projected areas of randomly rotated, simple, theoretical three-dimensional geometric solids (Fig  
281 3a). Shape parameters of the solids were quantified based on the edge-ratios, where  $x$  is the  
282 longest edge and  $x > y > z$ . Flatness ( $z/y$ ) and aspect ratios ( $y/x$ ) were chosen from 0.1 to 1 (0.1,  
283 0.5 and 1 combinations are presented in Fig 3b and Table 1), while the volume of the solids  
284 was kept constant at  $1 \mu\text{m}^3$ .

285 The XY-plane projected areas are dependent on two major factors: (1) rotation angles ( $\alpha_x$ ;  $\alpha_y$ );  
286 and (2) shape parameters (edge-ratios) of the objects. To determine the effect of rotation angles  
287 on projected areas, the  $\alpha_x$  and  $\alpha_y$  angles were modified from  $0^\circ$  to  $179^\circ$  and the projected areas  
288 were calculated for every rotation angle-pairs. The mean value of the rotation-dependent XY-  
289 plane projected areas is regarded as the orientation-averaged projected area representing  
290 randomly oriented object (gray surface on Fig 3c).

291 The introduced  $CE_{rot}$  ratio is the quotient of the largest face area-based CE diameter (it is  
292 assumed during the image analysis that this arbitrary orientation is set) and orientation-averaged  
293 projected area-based CE diameter (the projected area of a randomly oriented particle). Larger  
294 than 1  $CE_{rot}$  ratio values denote that the image analysis-based measurement overestimates  
295 particle size, while ratios  $< 1$  imply underestimation. These  $CE_{rot}$  ratios were calculated for every

296 possible aspect ratio-platyness combinations (Fig 4a). The displayed surface shows the level of  
297 overestimation as a function of shape parameters (orientation-averaged projected area). The  
298 higher the anisotropy of particles is, the higher the chance of overestimation of image analysis-  
299 based grain size measurement is.

300 Volume-based distribution curves were derived from the number-based database by weighting  
301 the individual particles with their sphere-equivalent volume, this assumption of spherical shape  
302 leads to further distortion of the results. Another correcting factor, the so-called CE/SE ratio  
303 was also introduced to reduce this inaccuracy of exchange transformation from number- to  
304 volume-based distribution functions, where SE diameters are equal for all modelled objects (as  
305 the volume of all these solids were defined as  $1 \mu\text{m}^3$ ). Similarly to  $\text{CE}_{\text{rot}}$  ratios, CE/SE ratios  
306 were specified for every possible aspect ratio-platyness combinations (Fig 4b), so mathematical  
307 relationships among the shape and rotation determined factors and aspect ratio-platyness values  
308 were assessed.

309 Aspect ratio of every single particle is known, which allowed us to get a more accurate 2-  
310 dimensional representation of 3-dimensional particles, only the particle thickness need to be  
311 estimated and the  $\text{CE}_{\text{rot}}$  and CE/SE correction factors can be determined for every investigated  
312 particles.

313

314 *Assessment of the 3<sup>rd</sup> dimension of particles: intensity based thickness assessment*

315

316 As a direct consequence of the previously discussed uncertainties, the major drawback of static  
317 automated image analysis is the unknown thickness of particles. To get an approximate  
318 estimation of the third-dimension, mean intensity values of the captured grayscale images were  
319 analysed in a completely novel way. Light transmission of sedimentary particles is influenced  
320 by thickness beyond mineral composition and colour. For this intensity based thickness

321 estimation method, average intensity values for all (n=101) grain size classes were determined  
322 and particles with an intensity being larger than the sum of their class intensity mean and  
323 standard deviation [ $\text{Int}_{\text{particle-ID}i} > \text{mean}(\text{Int}_{\text{GSbin-}j\text{th}}) + \sigma(\text{Int}_{\text{GSbin-}j\text{th}})$ ], where  $\text{Int}_{\text{particle-ID}i}$  is the  
324 intensity of *i*th particles from the *j*th size class,  $\text{mean}(\text{Int}_{\text{GSbin-}j\text{th}})$  and  $\sigma(\text{Int}_{\text{GSbin-}j\text{th}})$  are the  
325 average and standard deviation of the size class *j*] were classified as thinner (or flatter) than  
326 average ('platy') particles (Fig. 5). Later this classification of platy and more spherical particles  
327 was used during the mathematical adjustment with different assumptions for the 3rd dimension  
328 anisotropy (z/y: normal distribution for more spherical grains; z/y<0.1 for platy)

329

### 330 *Laser diffraction*

331

332 Additional grain size measurements were done using a Malvern Mastersizer 3000 laser  
333 diffraction device with Hydro LV unit to compare the new image analysis measurements with  
334 a widely used, traditional technique. There is a huge amount of published laser diffraction grain  
335 size data, however, only some of the research papers mention the drawbacks of these technique.  
336 In the case of middle and coarse silt-sized particles, majority of light is scattered by diffraction  
337 (the diffracted light has high intensity and low angle), while smaller particles refract and absorb  
338 more efficiently resulting a low intensity and wide angle scattered light. The acquired signal is  
339 transformed by the laser device software into particle size distribution data by using the  
340 Fraunhofer or the Mie scattering theory. Fraunhofer approximation is a simplified approach and  
341 the knowledge of refractive index and absorption coefficient is not required, since it is assumed  
342 that the measured particles are relatively large (over 25-30  $\mu\text{m}$  – about 40 times larger than the  
343 wavelength of the laser light) and opaque. More accurate particles size data can be gained by  
344 applying the Mie theory, however, as it is a solution for Maxwell's electromagnetic field  
345 equations the knowledge of optical properties (refractive index and absorption coefficient

346 [imaginary part of the complex refractive index]) of the sample and the dispersant is needed.  
347 Due to these reasons, Mie optical model provide more accurate data on the amount of smaller  
348 particles (clay and fine silt). As the knowledge of mineralogy-related optical properties is a  
349 mandatory for scattered light data to particle size Mie-transformations, bulk mineralogical  
350 composition of sediments was estimated from XRD data.

351 Previous XRD measurements of aeolian dust deposits in the Carpathian Basin indicated that  
352 quartz (~30-60%), 10Å phases (illite±muscovite±biotite: 20-30% in loess and 10-20% in  
353 paleosol), carbonates and 14Å phases (smectite±vermiculite±chlorite) were the dominant  
354 (Nemecz et al., 2000; Újvári et al., 2014). Bulk mineral composition data was used to assess  
355 the optimal optical settings of laser diffraction measurements to calculate grain size  
356 distributions by using the mineralogy-dependent complex refractive index: 1.54-0.1i for the  
357 sedimentary samples and 1.33 Ri for the dispersant water (Özer et al., 2010). However, due to  
358 the polymineral composition and dependence of absorption coefficient on particle shape and  
359 surface roughness, some additional calculations were made with the combination of various  
360 refractive indices (Ri: 1.45-1.6) and absorption coefficients (Ac: 0.01-1).

361

### 362 *Scanning electron microscopy*

363

364 Hitachi S-4300 CFE Scanning Electron Microscope (SEM) micrographs were taken to  
365 document and illustrate the shape and size variability of grains. SEM uses a focused beam of  
366 electrons to create magnified images being both high contrast and extremely sharp, and  
367 therefore suitable for particle surface morphology characterization. Previous studies reported  
368 that size and shape of individual particles can be accurately assessed by image analysis software  
369 and it is considered as a direct and absolute measure of particle size (Francus, 1998; Fandrich  
370 et al., 2007). In this paper, several tens of mineral particles per sample were pictured (with

371 magnification from 400× to 2000×) by SEM to confirm the notable irregular shape and  
372 anisotropy of 3<sup>rd</sup> dimension (thickness) of some particles.

373

## 374 **Results**

375

### 376 *Image analysis*

377

378 The acquired images of an average of 250,000 mineral particles per samples allowed us to  
379 calculate robust number- and volume-weighted size and shape distribution curves. Here, the  
380 grain size and intensity distributions are presented as both number and volume-based  
381 distributions, while other shape parameters are reported only as volume-weighted due to the of  
382 low-resolution of acquired images in the submicron fraction (<40 pixel) affecting the exact  
383 determination of particle perimeter (Fig 6 and Table 2).

384 Size and shape parameters of samples as well as their intensity values exhibit pretty similar  
385 general characteristics for the bulk, full grain size spectrums. The number size distributions  
386 have a general bimodal nature with a pronounced submicron peak and an additional one  
387 between 8 and 10 μm (Fig 6a). By contrast, the volume based CE diameter distributions are  
388 characterized with unimodal curves (closely log-normal distributions) with coarse silt-sized  
389 modal diameter values (40-60 μm) (Fig 6b).

390 As a logical consequence of number-based approach, most of the particles fall into the  
391 submicron fractions with high grayscale intensity values (due to their opacity) as it is reflected  
392 by the remarkable peak of the number-based intensity curve around the adjusted grayscale  
393 threshold of 144, what was selected to distinguish background from the mineral particles (Fig  
394 6c). Applying the volume-transformations by weighting the particles with their SE volume, the  
395 modal values were found in the darker range of grayscale intensity of 50 to 80 (Fig 6d).



396 General patterns of circularity and convexity distributions are resembling, both of these curves  
397 have a slight positive skewness (circularity: 1.2-2.3; convexity: 1.4-2.4) and modal values  
398 between 0.6 and 0.7 with tails extending towards more circular and convex shape directions  
399 (Fig 6e,f). Solidity of the mineral grains exhibits a rather homogeneous character with a clear  
400 positive skewness (3.1-4.5) and fairly high (>0.95) modulus (Fig 6g). Aspect ratios, being the  
401 ratios of width and length values, range dominantly between 0.7 and 0.9 (Fig 6h).

402 Granulometric parameters of selected size fractions were also analysed. Size and shape  
403 properties of clay (<2.00  $\mu\text{m}$ ), fine (2.00-6.25  $\mu\text{m}$ ), medium (6.25-20.00  $\mu\text{m}$ ) and coarse silt  
404 (20.00-62.50  $\mu\text{m}$ ) as well as of sand (larger than 62.5  $\mu\text{m}$ ) size particle classes were separately  
405 determined. A general granulometric heterogeneity was identified towards larger size fractions,  
406 so larger particles have a more irregular shape character than the finer ones. This heterogeneity  
407 is especially well expressed for circularity and convexity with mean values decreasing from  
408 0.95-0.97 to 0.64-0.71 from the clay to sand fractions. Similar, but not so obvious trends could  
409 be observed for the aspect ratio and solidity parameters. However, the aspect ratio values were  
410 fairly low even for the clay-sized grains (~0.78-0.8), translating to a 20-25% difference between  
411 particle length and width (Fig 7; Table 3).

412 Structural fingerprint analyses by Raman spectrometry aided mineral identifications. Due to the  
413 relatively low number of interpretable spectra, special focus was given to the main components  
414 of the samples studied (30-120  $\mu\text{m}$  quartz and feldspar grains). Size and shape parameters of  
415 these particle-clusters displayed similar main characteristics. All of the previously introduced  
416 parameters were found to be almost identical, only the mean intensities of quartz grains were  
417 biased towards lighter values compared to feldspars (Table 4).

418 Irregularity and heterogeneous shapes of sedimentary particles could undoubtedly be observed  
419 on the obtained SEM micrographs of bulk samples (Fig 8.). Acquired images also revealed  
420 several fracture faces, V-shaped percussion marks, linear steps, and conchoidal crushing

421 features on the grain surfaces. [According to Pye and Sperling (1983), Liu et al. (1985), Pye  
422 (1995), Lu et al. (2001) and Wright et al. (2011) this kind of morphological properties of silt-  
423 sized mineral grains are only characteristics of aeolian dust particles. Such microtextures  
424 together with the macroscopic characteristics of the silt classes indicate that these particles were  
425 primarily transported and deposited by wind, post-depositional alterations formed soils from  
426 this parent material.] The presence of fine-grained platy particles with significant 3<sup>rd</sup>  
427 dimensional anisotropy due to their thinness was also confirmed. However, the quantification  
428 of this anisotropy proved to be impossible using these images. Nevertheless, it is clear that  
429 thickness/width ratios are by orders of magnitude smaller than width/length ratios of some  
430 particles.

431

#### 432 *Laser diffraction*

433

434 Laser diffraction grain size measurements resulted in silt dominated, positively skewed  
435 (asymmetry towards the coarse fractions), unimodal distribution curves with minor, yet  
436 remarkable contribution of clay and fine-sand particles. The fine-grained tail into the direction  
437 of clay and fine silt fractions, beside the prominent maximum of medium- and coarse-silt  
438 components, is typical for aeolian dust deposits and paleosols intercalated in loess sequences.  
439 By using different complex refractive index values for grain size distribution measurements,  
440 the coarse silt-sized primary modes were not modified, however significant changes could be  
441 identified in the volumetric amount of clay and fine silt fractions (Fig 9).

442

#### 443 **Discussion**

444

445 *Sufficient number of measured particles*

446

447 It was found that, depending on the parameter itself, different particle numbers provide different  
448 representations of a sediment sample (Fig 10). For volume-based CE diameter distributions, the  
449 analyses of more than 50,000 particles are required to reach  $R^2=0.9$  between the total sample  
450 and the subpopulation (Fig 10a). However, since there is a cubic relationship between particle  
451 diameter and volume, even a small number of large (coarse silt and sand) particles is able to  
452 significantly modify the coarse grained tail of the grain size distribution. This apparent  
453 modification of the distribution curve cannot be easily quantified due to the logarithmic  
454 allocation of grain size bins. To get a more robust representation of grain size of polydisperse  
455 samples (particle sizes covering several orders of magnitude, e.g., submicron to some few  
456 hundred microns of aeolian dust deposits), several millions of scanned mineral particles would  
457 be necessary. At the same time, intensity or some shape parameters can be assessed fairly well  
458 using the results of only a few thousand particles (Fig 10b,c).

459

460 *Underestimation of the finest fractions by image analysis: a theoretical approach*

461

462 Image analysis grain size results indicated underestimation of clay and fine silt fractions  
463 compared to laser diffraction measurements, while the modal values of the coarse silt (or fine  
464 sand) fraction were found to be higher than those obtained by laser particle sizing.

465 By using  $CE_{rot}$  ratio and CE/SE corrections, the image analysis curves can be translated by a  
466 vector parallel to the x-axis by 10-15% assuming a normal distribution of thickness values.

467 Based on the SEM images and general character of clay-minerals, this latter assumption of  
468 normally distributed thickness values brings an obvious source of error into this correction  
469 process. By extending the modelling process towards thinner particles (with z/y ratios 0.01-  
470 0.09), the  $CE_{rot}$  ratio could result in more than a 50% correction on platy particle sizes.

471

472 *Combined application of modelled correction factors and intensity based thickness assessment*

473

474 Grain size and total volume of platy (more anisotropic) grains can be regarded as significantly  
475 overestimated as demonstrated by the previously deduced  $CE_{rot}$  (rotation averaged) ratio and  
476 CE/SE correction factor. The flatter than average particles were classified originally into larger  
477 grain size bins which therefore have an overestimated volume. Comparison of volumetric  
478 amount of bulk samples and particles classified based on intensities as ‘platy’ and ‘spherical’  
479 are shown in Fig 11. The introduced correction factors, even with the assumption of a normal  
480 distribution of particle thicknesses, are capable of making the CE diameters better converged,  
481 but unable to explain the larger size values themselves. The volumetric amount of more platy  
482 particles (especially clay minerals) is the most uncertain factor in these calculations, as a  
483 consequence of their significantly higher 3<sup>rd</sup> dimension anisotropy compared to the quartz and  
484 feldspar grains.

485 By applying the  $CE_{rot}$  ratio and CE/SE correction factor adjustment for the platy and spherical  
486 particles with different assumptions for the 3<sup>rd</sup> dimension anisotropy (z/y: normal distribution  
487 for spherical grains; <0.1 for platy), the results of laser diffraction and image analysis  
488 measurements are in better agreement, i.e., their correlation coefficients are higher compared  
489 to the original, mathematically “untreated” results.

490

## 491 **Conclusions**

492

493 Granulometric investigations of Pleistocene interglacial paleosols intercalated into loess  
494 sequences in the Carpathian Basin revealed the major discrepancies in results obtained by the  
495 two different measurement techniques applied. The data acquired by widely used, indirect laser

496 diffraction and direct observations by automated image analysis provided complementary, but  
497 different information on grain size. While the particle size distributions provided by laser  
498 diffraction measurements are dependent on the complex refractive index of a given particle  
499 (which can only be approximated in case of polymineral samples) assuming a spherical shape,  
500 the image analysis techniques are based simply on the direct, optically-acquired images of  
501 grains.

502 Comparisons of measured grain sizes indicated that the fine populations are consistently and  
503 significantly underestimated by the image analysis technique compared to laser scattering  
504 results. Modelling data demonstrate that the anisotropic character of irregular particles,  
505 especially the thickness of platy minerals, are responsible for the observed disagreements. The  
506 acquired two-dimensional images of dispersed particles sitting with their largest area on the  
507 glass slide were classified into grain size bins being too large based on their circle-equivalent  
508 diameter. In addition, their volumetric-weighting scores (sphere-equivalent volume derived  
509 from the CE diameter) were also found to be too high in volume-based conversions.  
510 Consequently, this led to overestimation of particle sizes and volumetric amounts of wrongly  
511 classified platy grains due to the cubic relationship. Application of the rotation averaged and  
512 SE/CE ratios as correction factors successfully reduces the discrepancies between results  
513 obtained by the two approaches. Nevertheless, the most definite factor, the unknown thickness  
514 of particles still remains an unresolved problem. The other presented innovative way of  
515 estimating the uncertain 3<sup>rd</sup> dimension of particles using their intensity-size relationships allows  
516 us to further minimize deviations between the two particle sizing methods.

517 However, since particle sizes of paleosols covering several orders of magnitude, even a small  
518 number of coarse grains can modify significantly the grain size distribution curves in the larger  
519 fractions distorting the whole measurement spectrum, and so the full agreement between laser  
520 diffraction and image analysis results cannot be reached.

521 There are discrepancies of these above discussed methods, but these can be handled by deeper  
522 understanding of physical background of them. Optical dependence of laser diffraction  
523 measurements should be investigated in the future, while the thickness-related uncertainties of  
524 image analysis must also be studied by further studies. All in all, there are uncertainties  
525 connected to both approaches, however, these two methods can be important complements of  
526 each other, providing a useful tool to decipher valuable sedimentary information from  
527 granulometric data of various deposits.

528

### 529 **Acknowledgement**

530

531 Support of the National Research, Development and Innovation Office NKFIH K120620 (for  
532 G. Varga) and K120213 (for J. Kovács) are gratefully acknowledged. It was additionally  
533 supported (for G. Varga) by the Bolyai János Research Scholarship of the Hungarian Academy  
534 of Sciences.

535

### 536 **References**

537

538 Altuhafi, F., O'Sullivan, C., Cavarretta, I., 2013. Analysis of an image-based method to quantify  
539 the size and shape of sand particles. *Journal of Geotechnical and Geoenvironmental*  
540 *Engineering* 139, 1290-1307.

541 Bagheri, G.H., Bonadonna, C., Manzella, I., Vonlanthen, P., 2015. On the characterization of  
542 size and shape of irregular particles. *Powder Technology*, 141-153.

543 Baptista, P., Cunha, T.R., Gama, C., Bernardes, C., 2012. A new and practical method to obtain  
544 grain size measurements in sandy shores based on digital image acquisition and processing.  
545 *Sedimentary Geology* 282, 294-306.

546 Becker, L.W.M., Hjelstuen, B.O., Støren, E.W.N., Sejrup, H.P., in press. Automated counting  
547 of sand-sized particles in marine records. *Sedimentology*.

548 Benn, D.I., Ballantyne, C.K., 1993. The description and representation of particle shape. *Earth*  
549 *Surface Processes and Landforms* 18, 665-672.

550 Buscombe, D., Rubin, D.M., Warrick, J.A., 2010. A universal approximation of grain size from  
551 images of noncohesive sediment. *Journal of Geophysical Research: Earth Surface* 115, F02015.

552 Campaña, I., Benito-Calvo, A., Pérez-González, A., Bermúdez de Castro, J.M., Carbonell, E.,  
553 2016. Assessing automated image analysis of sand grain shape to identify sedimentary facies,  
554 Gran Dolina archaeological site (Burgos, Spain). *Sedimentary Geology* 346, 72-83.

555 Dellino, P., La Volpe, L., 1996. Image processing analysis in reconstructing fragmentation and  
556 transportation mechanisms of pyroclastic deposits. The case of Monte Pilato-Rocche Rosse  
557 eruptions, Lipari (Aeolian islands, Italy). *Journal of Volcanology and Geothermal Research* 71,  
558 13-29.

559 Di Stefano C, Ferro V, Mirabile S., 2010. Comparison between grain-size analyses using laser  
560 diffraction and sedimentation methods. *Biosystems Engineering* 106, 205-215.

561 Duval, M., Campana, I., Guilarte, V., Miguens, L., Iglesias, J., Sierra, S.G., 2015. Assessing  
562 the uncertainty on particle size and shape: Implications for ESR and OSL dating of quartz and  
563 feldspar grains. *Radiation Measurements* 81, 116-122.

564 Fandrich, R., Gu, Y., Burrows, D., Moeller, K., 2007. Modern SEM-based mineral liberation  
565 analysis. *International Journal of Mineral Processing* 84, 310-320.

566 Fisher, P., Aumann, C., Chia, K., O'Halloran, N., Chandra, S., 2017. Adequacy of laser  
567 diffraction for soil particle size analysis. *PLoS ONE* 12, 0176510

568 Francus, P., 1998. An image-analysis technique to measure grain-size variation in thin sections  
569 of soft clastic sediments. *Sedimentary Geology* 121, 289-298.

570 Gamble, J.F., Chiu, W.S., Tobyn, M., 2011. Investigation into the impact of sub-populations of  
571 agglomerates on the particle size distribution and flow properties of conventional  
572 microcrystalline cellulose grades. *Pharmaceutical Development and Technology* 16, 542-548.

573 Gamble, J.F., Ferreira, A.P., Tobyn, M., DiMemmo, L., Martin, K., Mathias, N., Schild, R.,  
574 Vig, B., Baumann, J.M., Parks, S., Ashton, M., 2014. Application of imaging based tools for  
575 the characterisation of hollow spray dried amorphous dispersion particles. *International Journal*  
576 *of Pharmaceutics* 465, 210-217.

577 Graham, D.J., Rice, S.P., Reid, I., 2005. A transferable method for the automated grain sizing  
578 of river gravels. *Water Resources Research* 41, 1-12.

579 Konert, M., Vandenberghe, J., 1997. Comparison of laser grain size analysis with pipette and  
580 sieve analysis: A solution for the underestimation of the clay fraction. *Sedimentology* 44, 523-  
581 535.

582 Kwan, A.K.H., Mora, C.F., Chan, H.C., 1999. Particle shape analysis of coarse aggregate using  
583 digital image processing. *Cement and Concrete Research* 29, 1403-1410.

584 Leibrandt, S., Le Pennec, J.L., 2015. Towards fast and routine analyses of volcanic ash  
585 morphometry for eruption surveillance applications. *Journal of Volcanology and Geothermal*  
586 *Research* 297, 11-27.

587 Lisiecki, L., Raymo, M.E., 2005. A Pliocene–Pleistocene stack of 57 globally distributed  
588 benthic  $\delta^{18}\text{O}$  records. *Paleoceanography* 20, PA1003. DOI: 10.1029/2004PA001071

589 Liu, E.J., Cashman, K.V., Rust, A.C., 2015. Optimising shape analysis to quantify volcanic ash  
590 morphology. *GeoResJ* 8, 14-30.

591 Lu, H., Vandenberghe, J., 2001. Aeolian origin and palaeoclimatic implications of the 'Red  
592 Clay' (north China) as evidenced by grain-size distribution. *Journal of Quaternary Science* 16,  
593 89-97.



594 Ludwick, J.C., Henderson, P.L. 1968. Particle shape and inference of size from sieving.  
595 *Sedimentology* 11, 197-235.

596 Makó, A., Tóth, G., Weynants, M., Rajkai, K., Hermann, T., Tóth, B., 2017. Pedotransfer  
597 functions for converting laser diffraction particle-size data to conventional values. *European*  
598 *Journal of Soil Science* 68, 769-782.

599 Malvern Instruments Ltd., 2015. Morphologi G3 User Manual. Malvern, United Kingdom, 268  
600 p.

601 Mazzullo, J. M., Alexander, A., Tieh, T., Menglin, D., 1992. The effects of wind transport on  
602 the shapes of quartz silt grains. *Journal of Sedimentary Petrology* 62, 961-971.

603 Nemeč, E., Pécsi, M., Hartyáni, Z., Horváth, T., 2000. The origin of the silt size quartz grains  
604 and minerals in loess. *Quaternary International* 67-71, 199-208.

605 Nielsen, P.R., Dahl, S.O., Jansen, H.L., Støren, E.N., 2016. Holocene aeolian sedimentation  
606 and episodic mass-wasting events recorded in lacustrine sediments on Langøya in Vesterålen,  
607 northern Norway. *Quaternary Science Reviews* 148, 146-162.

608 Oches, E.A., McCoy, W.D., 1995. Aminostratigraphic evaluation of conflicting age estimates  
609 for the “young loess” of Hungary. *Quaternary Research* 44, 160-170.

610 Özer, M., Orhan, M., Işık, N.S., 2010. Effect of particle optical properties on size distribution  
611 of soils obtained by laser diffraction. *Environmental and Engineering Geoscience*. 16,163-73.

612 Polakowski, C., Sochan, A., Bieganski, A., Ryzak, M., Földényi, R., Tóth, J., 2014.  
613 Influence of the sand particle shape on particle size distribution measured by laser diffraction  
614 method. *International Agrophysics* 28, 195-200.

615 Polo-Díaz, A., Benito-Calvo, A., Martínez-Moreno, J., Mora Torcal, R., 2016. Formation  
616 processes and stratigraphic integrity of the Middle-to-Upper Palaeolithic sequence at Cova  
617 Gran de Santa Linya (Southeastern Prepyrenees of Lleida, Iberian Peninsula). *Quaternary*  
618 *International* 417, 16-38.

619 Pye, K.H., Sperling, C.H.B., 1983. Experimental investigation of silt formation by static  
620 breakage processes: the effect of temperature, moisture and salt on quartz dune sand and  
621 granitic regolith. *Sedimentology* 30, 49-62.

622 Pye, K., 1987. *Aeolian Dust and Dust Deposits*. Academic Press, London 334 p.

623 Pye, K., 1994. Shape sorting during wind transport of quartz silt grains - discussion. *Journal of*  
624 *Sedimentary Research A* 64, 704-705.

625 Pye, K., 1995. The nature, origin and accumulation of loess. *Quaternary Science Reviews* 14,  
626 653-667.

627 Rodríguez, J.M., Edeskär, T., Knutsson, S., 2013. Particle shape quantities and measurement  
628 techniques-A review. *Electronic Journal of Geotechnical Engineering* 18 A, 169-198.

629 Rubin, D.M., 2004. A simple autocorrelation algorithm for determining grain size from digital  
630 images of sediment. *Journal of Sedimentary Research* 74, 160-165.

631 Schneider, A., Marcini, A., 2013. Morphologi G3-ID - A new instrument for problems in  
632 cement research. *Cement International* 11, 69-77.

633 Schulte, P., Lehmkuhl, F., in press. The difference of two laser diffraction patterns as an  
634 indicator for post-depositional grain size reduction in loess-paleosol sequences.  
635 *Palaeogeography, Palaeoclimatology, Palaeoecology*

636 Schulte, P., Sprafke, T, Rodrigues, L., Fitzsimmons, K.E., in press. Are fixed grain size ratios  
637 useful proxies for loess sedimentation dynamics? Experiences from Remizovka, Kazakhstan.  
638 *Aeolian Research*

639 Shang, Y., Kaakinen, A., Beets, C.J., Prins, M.A., in press. Aeolian silt transport processes as  
640 fingerprinted by dynamic image analysis of the grain size and shape characteristics of Chinese  
641 loess and Red Clay deposits. *Sedimentary Geology*.

642 Sochan, A., Zieliński, P., Bieganski, A., 2015. Selection of shape parameters that  
643 differentiate sand grains, based on the automatic analysis of two-dimensional images.  
644 *Sedimentary Geology* 327, 14-20.

645 Tafesse, S., Robison Fernlund, J.M., Sun, W., Bergholm, F., 2013. Evaluation of image analysis  
646 methods used for quantification of particle angularity. *Sedimentology* 60, 1100-1110.

647 Újvári, G., Varga, A., Raucsik, B., Kovács, J., 2014. The Paks loess-paleosol sequence: A  
648 record of chemical weathering and provenance for the last 800ka in the mid-Carpathian Basin.  
649 *Quaternary International* 319, 22-37.

650 Újvári, G., Kok, J.F., Varga, G., Kovács, J., 2016. The physics of wind-blown loess:  
651 Implications for grain size proxy interpretations in Quaternary paleoclimate studies. *Earth-*  
652 *Science Reviews* 154, 247-278.

653 Ulusoy, U., Kursun, I., 2011. Comparison of different 2D image analysis measurement  
654 techniques for the shape of talc particles produced by different media milling. *Minerals*  
655 *Engineering* 24, 91-97.

656 van Hateren, J.A., Prins, M.A., van Balen, R.T., in press. On the genetically meaningful  
657 decomposition of grain-size distributions: A comparison of different end-member modelling  
658 algorithms. *Sedimentary Geology*

659 Vandenberghe, J., 2013. Grain size of fine-grained windblown sediment: A powerful proxy for  
660 process identification. *Earth-Science Reviews* 121, 18-30.

661 Varga, G., 2015. Changing nature of pleistocene interglacials—is it recorded by paleosoils in  
662 Hungary (Central Europe)? *Hungarian Geographical Bulletin* 64, 313-322.

663 Varga, G., Cserhádi, Cs., Kovács, J., Szalai, Z., 2016. Saharan dust deposition in the Carpathian  
664 Basin and its possible effects on interglacial soil formation. *Aeolian Research* 22, 1-12.

665 Varga, Gy., Újvári, G., Kovács, J., in press. Interpretation of sedimentary (sub)populations  
666 extracted from grain size distributions of Central European loess-paleosol series. *Quaternary*  
667 *International*

668 Warrick, J.A., Rubin, D.M., Ruggiero, P., Harney, J.N., Draut, A.E., Buscombe, D., 2009.  
669 Cobble cam: Grain-size measurements of sand to boulder from digital photographs and  
670 autocorrelation analyses. *Earth Surface Processes and Landforms* 34, 1811-1821.

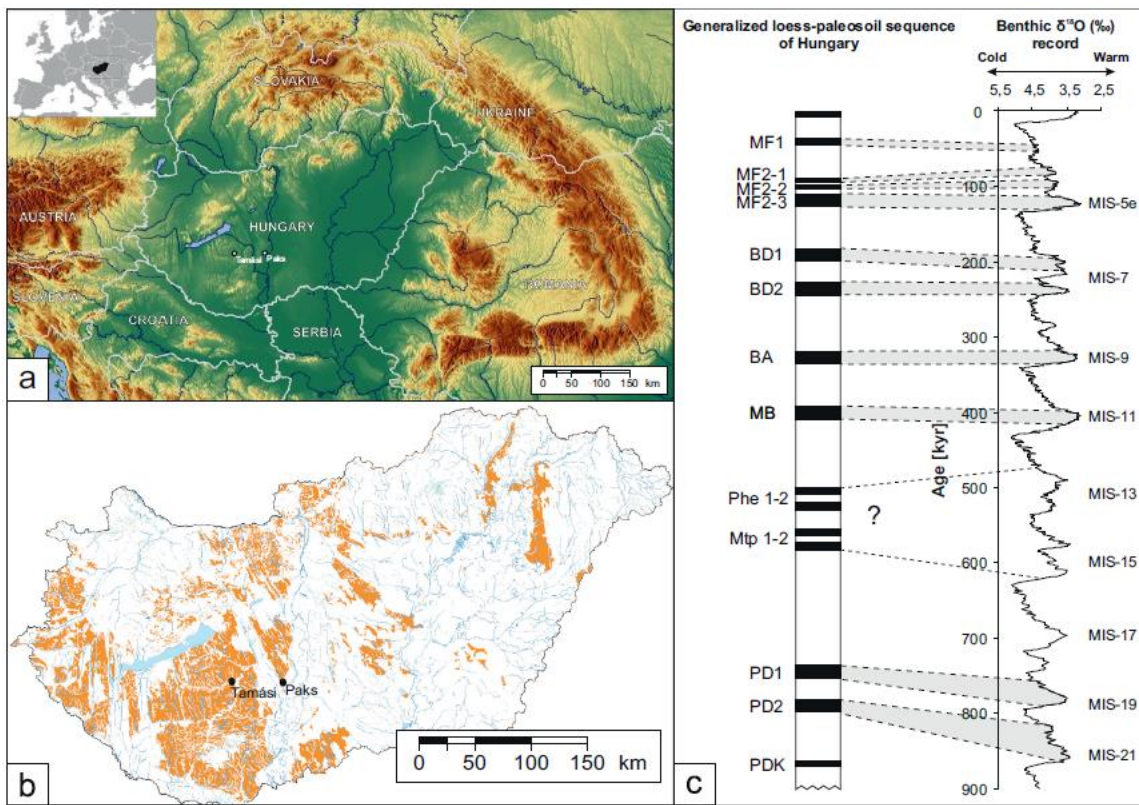
671 Wright, J.S., 2001. Desert loess versus glacial loess: Quartz silt formation, source areas and  
672 sediment pathways in the formation of loess deposits. *Geomorphology* 36, 231-256.

673

674

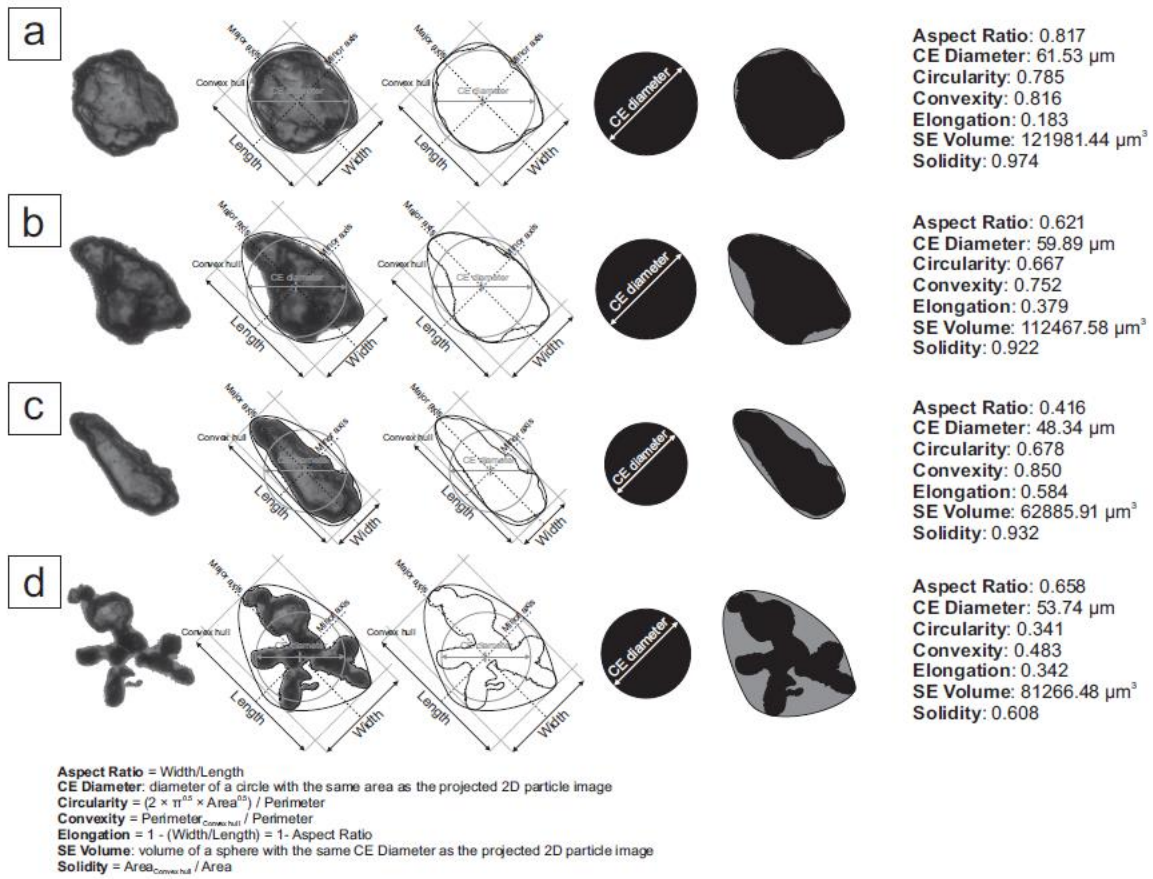
675

676 **Figures:**



677  
 678 Figure 1. Origin of samples: (a) location map of investigated sites in the Carpathian Basin; (b)  
 679 loess distribution map of Hungary; (c) generalized loess-paleosol sequence of Hungary and its  
 680 possible correlation with benthic  $\delta^{18}O$  record of deep sea sediments (Lisiecki and Raymo,  
 681 2005).

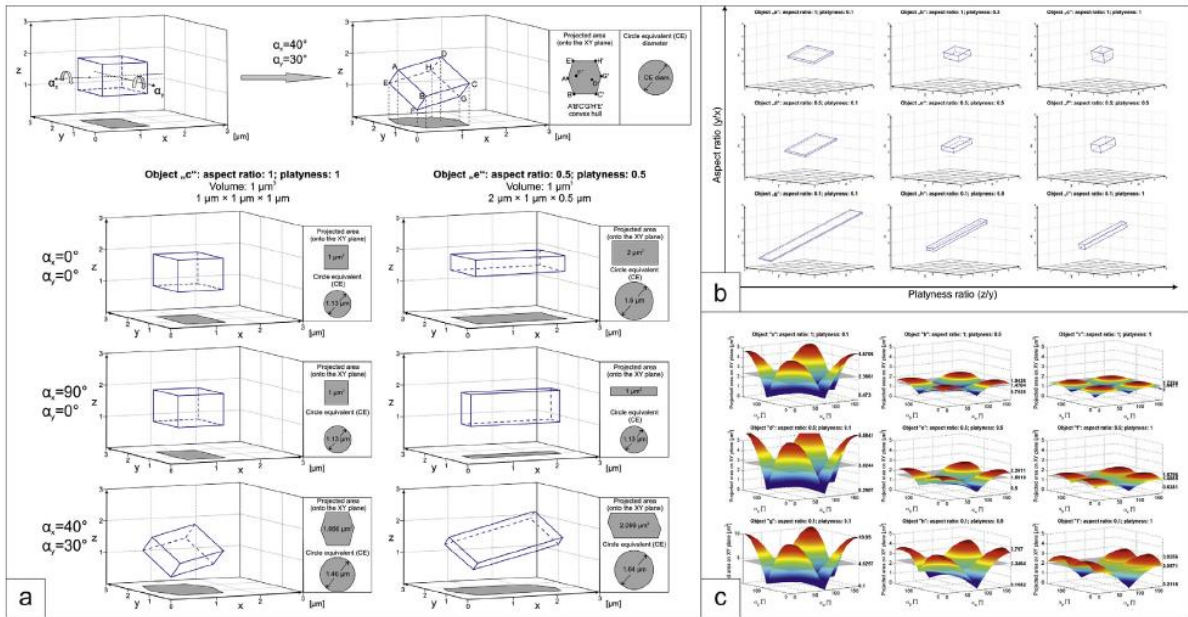
682



683

684 Figure 2. Schematic illustration of major grain size and shape parameters of irregular mineral  
 685 particles (from a to d examples refer to more irregular shapes; gray areas represent the convex  
 686 hull).

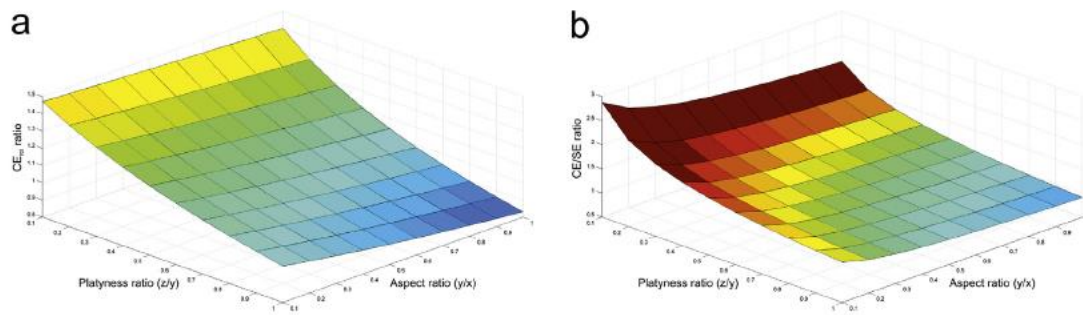
687



688

689 Figure 3. Assessment of projected area of a randomly oriented geometric objects: (a) general  
 690 problem of shape and rotation determined projected area; (b) presented nine simple geometric  
 691 objects; (c) rotation averaged projected areas as a function of rotation angles.

692



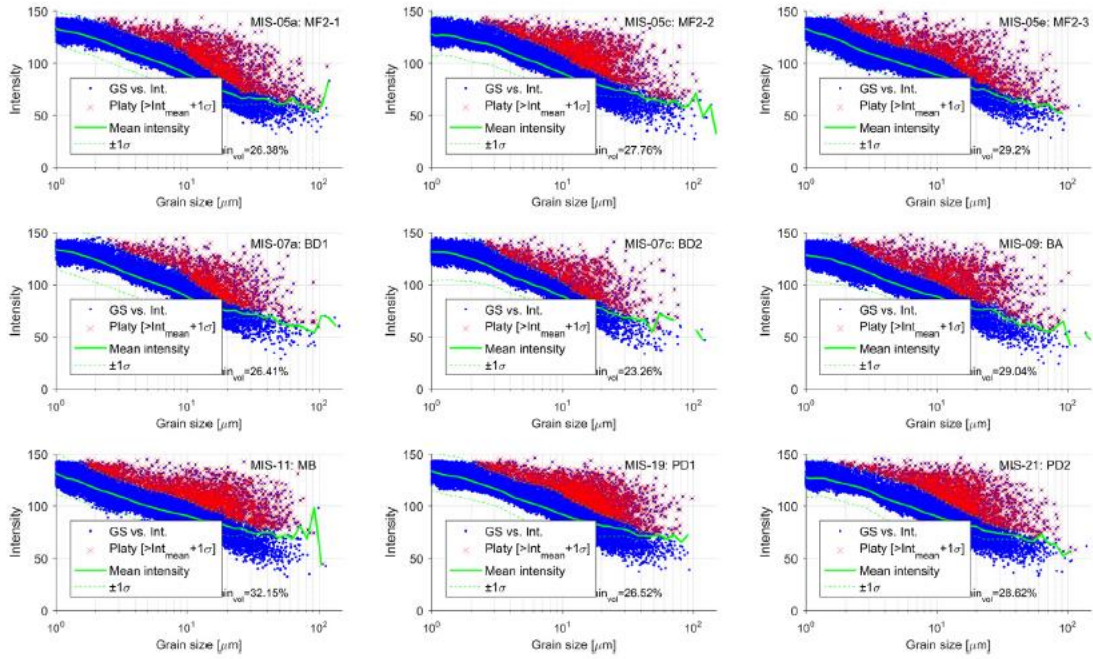
693

694 Figure 4. The introduced (a)  $CE_{rot}$  and (b)  $CE/SE$  ratios as a function of aspect and platyness

695 ratios of simple objects.

696

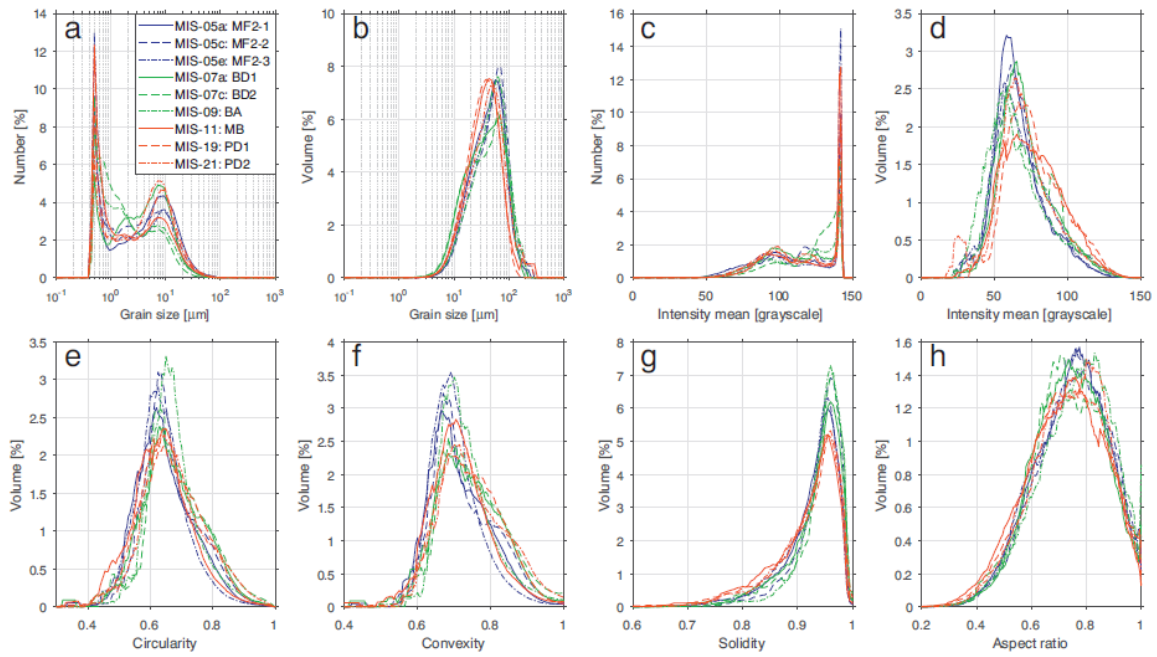




697

698 Figure 5. Assessment of amount of platy mineral particles from the grain size vs. grayscale  
 699 intensity scatter plots.

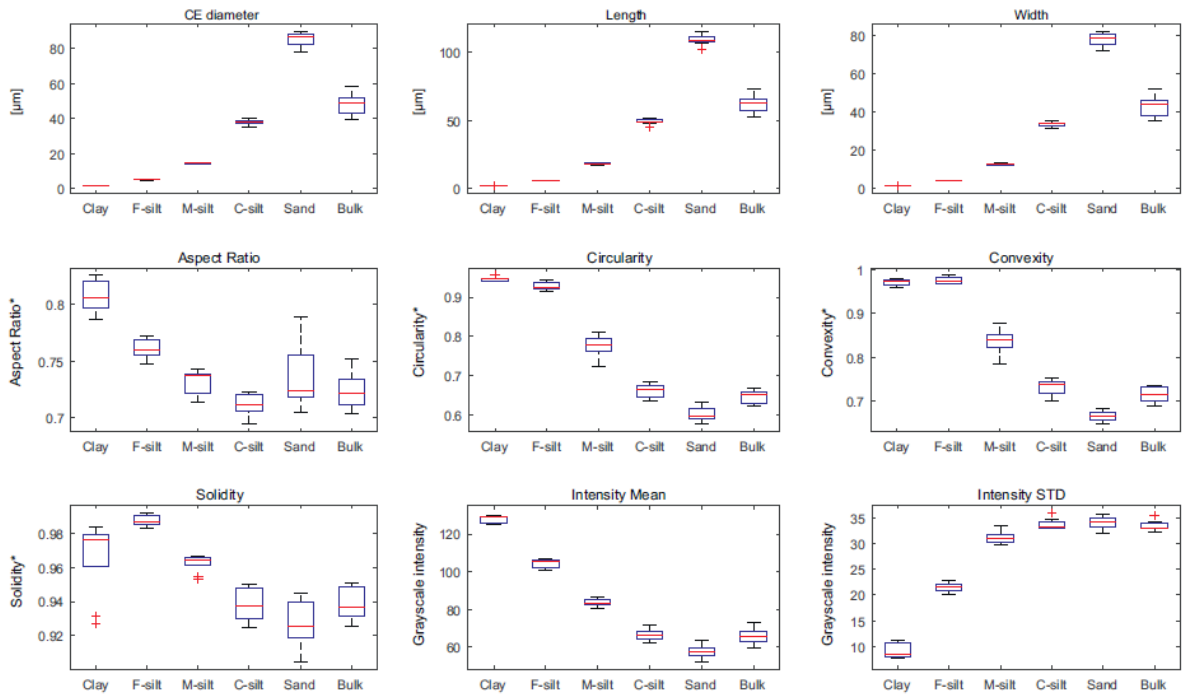
700



701

702 Figure 6. Grain size and shape parameter distributions of the investigated samples (a: number-  
 703 based grain size distribution; b: volume-based grain size distribution; c: number-based  
 704 grayscale intensity distribution; d: volume-based grayscale intensity distribution; e: volume-  
 705 based circularity distribution; f: volume-based convexity distribution; g: volume-based solidity  
 706 distribution; h: volume-based aspect ratio distribution).

707



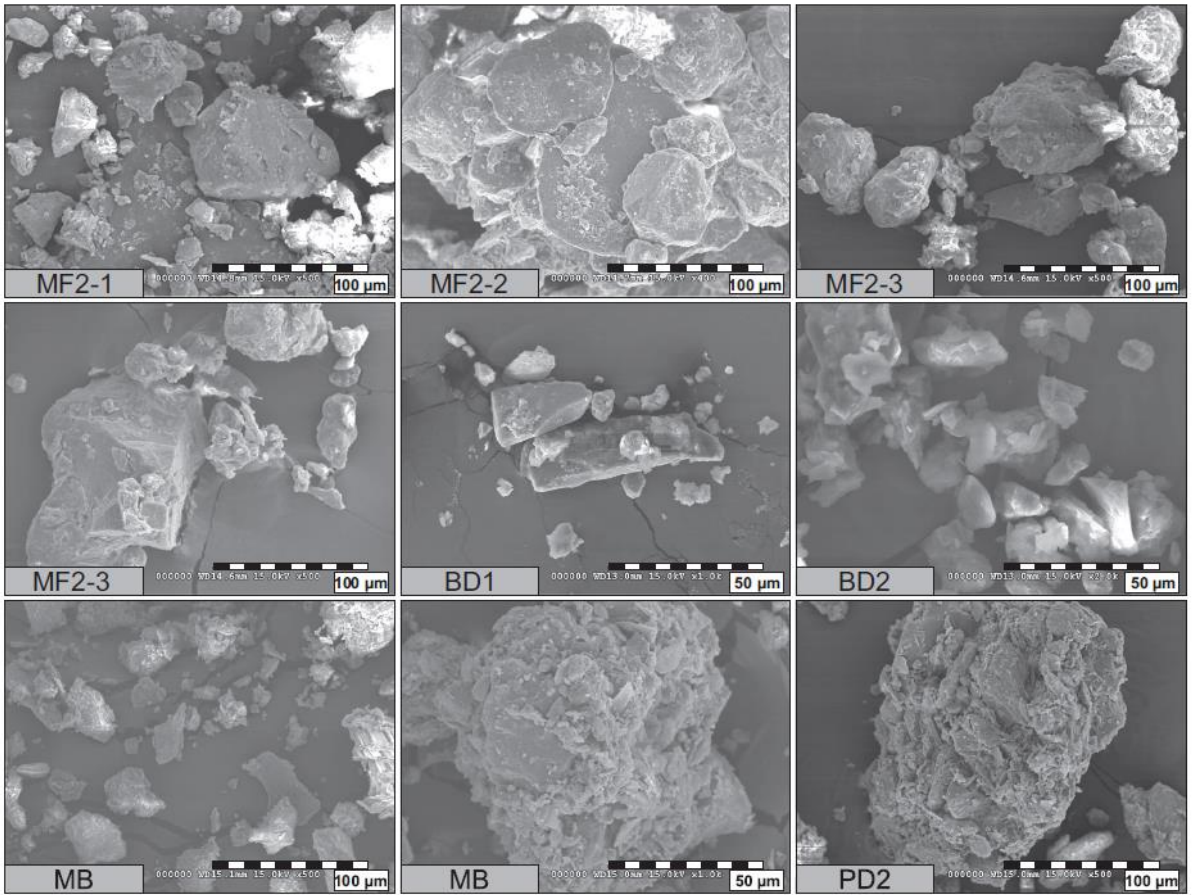
708

709 Figure 7. Box-plots of various granulometric parameters by size fractions (CE diameter: circle-

710 equivalent diameter; clay:  $<2.00 \mu\text{m}$ ; F-silt [fine silt]:  $2.00\text{-}6.25 \mu\text{m}$ ; M-silt [medium silt]:  $6.25\text{-}$

711  $20.00 \mu\text{m}$ ; C-silt [coarse silt]  $20.00\text{-}62.50 \mu\text{m}$ ; sand: larger than  $62.5 \mu\text{m}$ ).

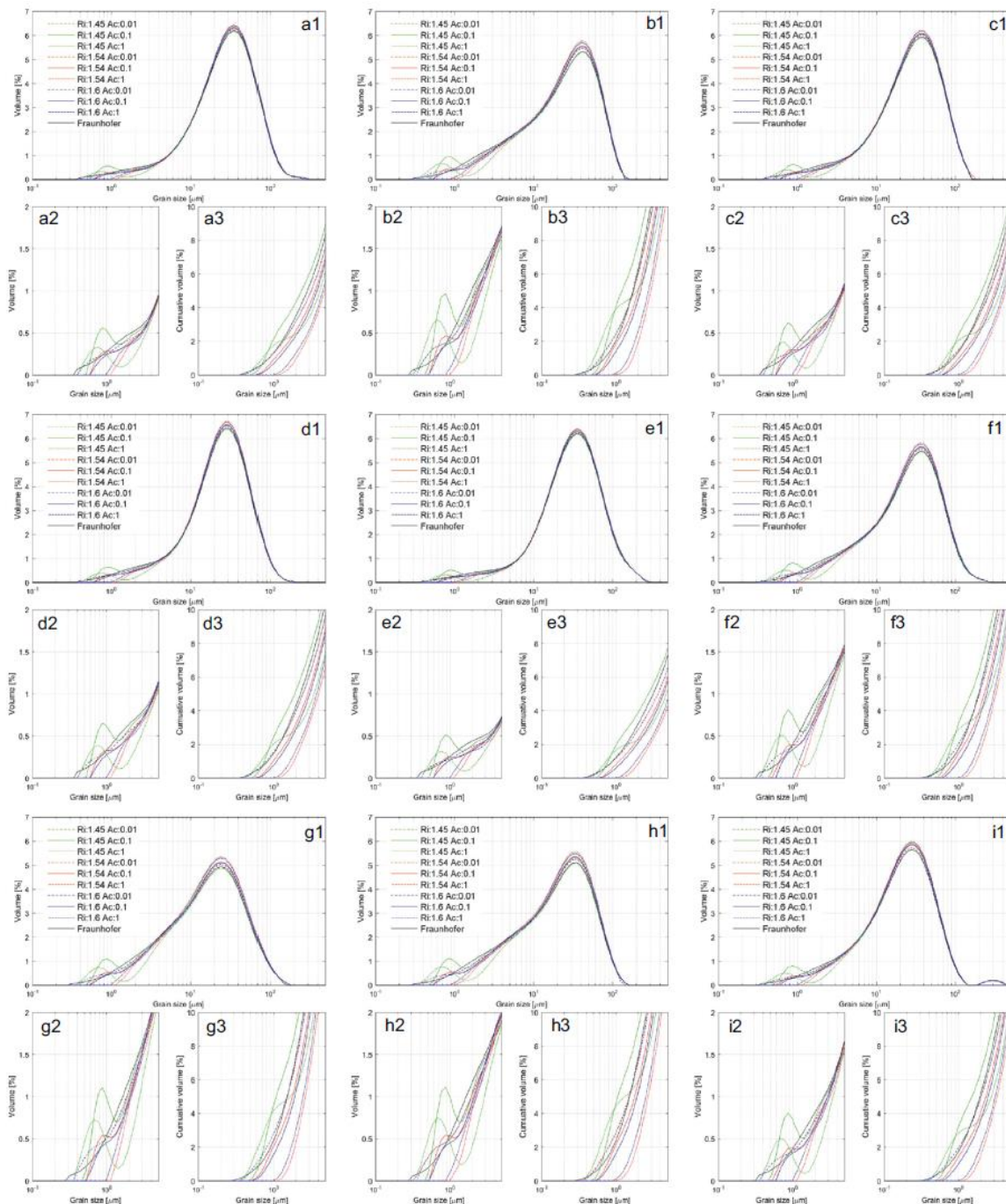
712



713

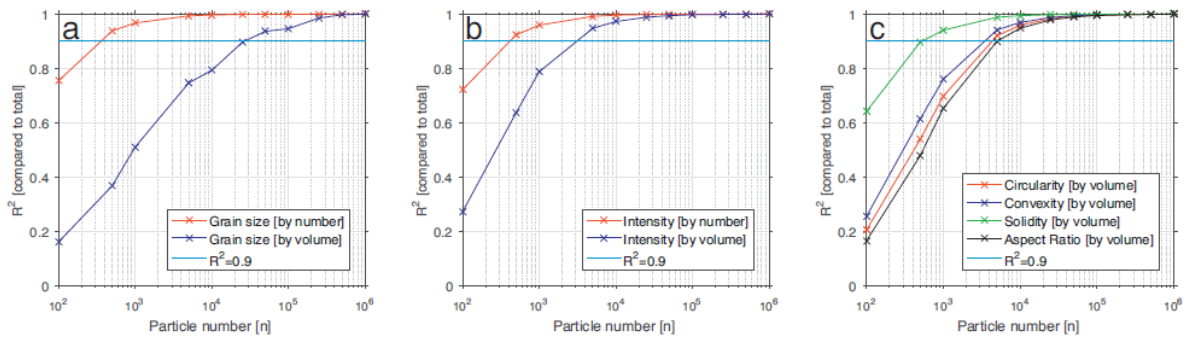
714 Figure 8. Scanning electron micrographs of paleosol samples.

715



716

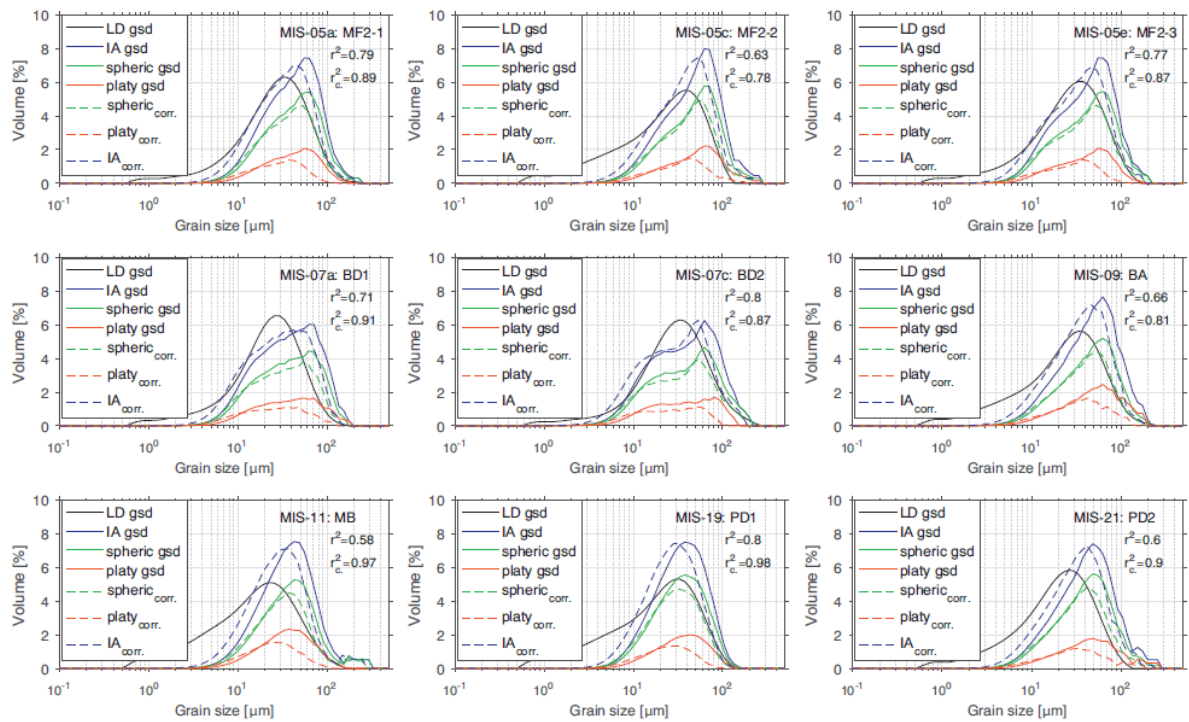
717 Figure 9. Laser diffraction grain size distributions of paleosol samples by using different  
 718 complex refractive indices (a-i refer to investigated samples [a: MF2-1; b: MF2-2; c: MF2-3;  
 719 d: BD-1; e: BD-2; f: BA; g: MB; h: PD1; i: PD2]; while numbers indicate the distribution types:  
 720 1: grain size distribution of the whole size spectrum [0.1-500  $\mu\text{m}$ ]; 2: grain size distribution of  
 721 fine-grained fractions [0.1-50  $\mu\text{m}$ ]; 3: cumulative grain size distribution of the fine-grained  
 722 fractions [0.1-50  $\mu\text{m}$ ]).



723

724 Figure 10. Relationship between number of scanned particles and representativeness of various  
 725 granulometric parameters (a: number- and volume-based grain size; b: number- and volume-  
 726 based grayscale intensity; c: volume-based circularity, convexity, solidity and aspect ratio) for  
 727 the whole samples.

728



729

730 Figure 11. Grain size distributions of laser diffraction, image analysis and corrected image  
 731 analysis measurements (LD gsd: laser diffraction grain size distribution; IA gsd: image analysis  
 732 grain size distribution; ‘corr’ subscripts refer to corrected values).

733

734

735 Table 1. General size and shape characteristics of the presented geometric objects and derived  
 736 correction factors.

ID	Shape parameters		Edge lengths			Volume		Largest face		Projected areas on XY plane								CE <sub>rot</sub> ratio <sup>c</sup>	CE/SE ratio <sup>d</sup>
	Aspect ratio (y/x)	Platyness (z/y)	x	y	z	[ $\mu\text{m}^3$ ]	SE <sup>a</sup> diameter	Area	CE <sup>b</sup> diameter	Areas				CE diameters					
										min	max	mean	std	min	max	mean	std		
a	1	0.1	2.15	2.15	0.22	1	1.24	4.64	2.43	0.47	4.67	2.37	1.26	0.78	2.44	1.74	0.48	1.40	1.96
b	1	0.5	1.26	1.26	0.63	1	1.24	1.59	1.42	0.79	1.94	1.47	0.32	1.01	1.57	1.37	0.16	1.04	1.15
c	1	1	1.00	1.00	1.00	1	1.24	1.00	1.13	1.00	1.72	1.45	0.18	1.13	1.48	1.36	0.09	0.83	0.91
d	0.5	0.1	3.42	1.71	0.17	1	1.24	5.85	2.73	0.29	5.88	2.82	1.65	0.61	2.74	1.90	0.59	1.44	2.20
e	0.5	0.5	2.00	1.00	0.50	1	1.24	2.00	1.60	0.50	2.29	1.59	0.51	0.80	1.71	1.42	0.25	1.12	1.29
f	0.5	1	1.59	0.79	0.79	1	1.24	1.26	1.27	0.62	1.88	1.49	0.34	0.89	1.55	1.38	0.17	0.92	1.02
g	0.1	0.1	10.00	1.00	0.10	1	1.24	10.00	3.57	0.10	10.05	4.63	2.90	0.36	3.58	2.43	0.84	1.47	2.88
h	0.1	0.5	5.85	0.58	0.29	1	1.24	3.42	2.09	0.17	3.80	2.35	1.04	0.46	2.20	1.73	0.44	1.21	1.68
i	0.1	1	4.64	0.46	0.46	1	1.24	2.15	1.66	0.21	3.03	2.09	0.80	0.52	1.96	1.63	0.37	1.02	1.34

<sup>a</sup> SE: sphere-equivalent.

<sup>b</sup> CE: circle-equivalent.

<sup>c</sup> CE<sub>rot</sub> ratio: ratio of the largest face area-based CE diameter.

<sup>d</sup> CE/SE ratio: ratio of SE and CE diameters.

737

738



739

740 Table 2. Mean grain size and shape parameters of the investigated samples.

Sample Name	CE diam. [µm]	Clay [vol.%]	Fine silt [vol.%]	Medium silt [vol.%]	Coarse silt [vol.%]	Sand [vol.%]	Length [µm]	Width [µm]	Aspect Ratio	Circularity	Convexity	Solidity	Intensity Mean	Intensity STD
MIS-05a [MF2-1]	49.83	0.01	0.31	12.46	49.33	37.90	64.19	44.43	0.73	0.63	0.69	0.94	62.09	35.47
MIS-05c [MF2-2]	58.19	0.01	0.36	10.77	42.52	46.34	72.80	52.01	0.74	0.64	0.70	0.95	63.53	32.97
MIS-05e [MF2-3]	50.40	0.02	0.42	15.20	45.35	39.02	64.46	45.03	0.72	0.62	0.69	0.94	63.14	33.81
MIS-07a [BD1]	42.91	0.02	0.75	19.81	45.18	34.25	56.20	38.77	0.72	0.65	0.73	0.94	66.53	34.08
MIS-07c [BD2]	45.68	0.06	1.02	20.38	40.66	37.88	57.05	40.48	0.71	0.67	0.74	0.95	65.64	32.94
MIS-09 [BA]	54.89	0.02	0.46	11.67	45.16	42.69	69.71	48.73	0.75	0.66	0.72	0.95	59.66	32.26
MIS-11 [MB]	42.57	0.02	0.48	14.57	57.25	27.68	56.96	38.03	0.70	0.63	0.71	0.93	72.81	32.82
MIS-19 [PD1]	39.75	0.01	0.37	15.91	60.09	23.61	52.26	35.71	0.71	0.65	0.73	0.93	73.17	32.95
MIS-21 [PD2]	49.09	0.01	0.46	13.75	50.81	34.98	63.07	44.38	0.72	0.66	0.73	0.93	66.57	32.99
Mean	47.35	0.01	0.41	13.40	51.42	34.76	61.47	42.48	0.72	0.64	0.71	0.94	66.65	33.22
STD	6.02	0.02	0.23	3.36	6.58	7.02	6.77	5.29	0.02	0.02	0.02	0.01	4.59	0.96

741

742

743 Table 3. Mean values of various granulometric parameters by size fractions.

Fractions	CE diam. [ $\mu\text{m}$ ]	Length [ $\mu\text{m}$ ]	Width [ $\mu\text{m}$ ]	Aspect Ratio	Circularity	Convexity	Solidity	Intensity Mean	Intensity STD
Clay (<2 $\mu\text{m}$ )	1.51	1.84	1.44	0.80	0.95	0.97	0.97	127.00	9.80
Fine silt (2–6.25 $\mu\text{m}$ )	5.09	6.12	4.47	0.76	0.93	0.98	0.99	104.10	21.68
Medium silt (6.25–20 $\mu\text{m}$ )	14.78	18.39	12.89	0.73	0.77	0.84	0.96	84.00	30.86
Coarse silt (20–62.5 $\mu\text{m}$ )	38.56	49.90	34.34	0.71	0.66	0.73	0.94	67.25	33.49
Sand (>62.5 $\mu\text{m}$ )	82.93	107.50	76.28	0.74	0.60	0.66	0.93	57.29	33.69
Bulk	47.35	61.47	42.48	0.72	0.64	0.71	0.94	66.65	33.22

744

745

746

747 Table 4. Shape parameters of 30-120  $\mu\text{m}$  quartz, feldspar and bulk samples.

Samples [30-120 $\mu\text{m}$ ]	Aspect Ratio	Circularity	Convexity	Solidity	Intensity mean	Intensity STD
Quartz	0.7361	0.6133	0.6762	0.9284	60.3	33.29
Feldspar	0.7164	0.6136	0.6846	0.929	56.57	33.61
Bulk	0.7208	0.6245	0.6922	0.929	62.24	33.57

748

749